Geophysical Journal International

Geophys. J. Int. (2025) **241**, 863–875
Advance Access publication 2025 February 26
GJI Seismology

https://doi.org/10.1093/gji/ggaf076

Comprehensive global data set of uniformly processed shear-wave splitting measurements

Jonathan Wolf,[1,2] Thorsten W. Becker,[3,4,5] Edward Garnero,[6] Kelly H. Liu[7] and John D. West[6]

[1]*Department of Earth and Planetary Science, University of California, Berkeley, CA* 94720, *USA. E-mail: jonathan.wolf@berkeley.edu*
[2]*Miller Institute for Basic Research in Science, Berkeley, CA* 94720, *USA*
[3]*Institute for Geophysics, Jackson School of Geosciences, The University of Texas at Austin, Austin,TX* 78712, *USA*
[4]*Department of Earth and Planetary Sciences, Jackson School of Geosciences, The University of Texas at Austin, Austin,TX* 78712, *USA*
[5]*Oden Institute for Computational Engineering & Sciences, The University of Texas at Austin, Austin,TX* 78712, *USA*
[6]*School of Earth and Space Exploration, Arizona State University, Tempe, AZ* 85287, *USA*
[7]*Department of Earth Sciences and Engineering, Missouri University of Science and Technology, Rolla, MO* 65409, *USA*

Accepted 2025 February 22. Received 2025 February 13; in original form 2024 December 6

SUMMARY

Seismic anisotropy can inform us about convective flow in the mantle. Shear waves traveling through azimuthally anisotropic regions split into fast and slow pulses, and measuring the resulting shear-wave splitting provides some of the most direct insights into Earth's interior dynamics. Shear-wave splitting is a constraint for path-averaged azimuthal anisotropy and is often studied regionally. Global compilations of these measurements also exist. Such compilations include measurements obtained using different data processing methodologies (e.g., filtering), which do not necessarily yield identical results, and reproducing a number of studies can be challenging given that not all provide the required information, for example, about the source location. Here, we automatically determine shear-wave splitting parameters from core-refracted SKS, SKKS and PKS waves from a global data set. This data set includes all earthquakes with magnitudes $\geq$ 5.9 from 2000 to the present, collected from 24 data centers, totaling over 4700 events and 16 million three-component seismograms. We obtain approximately 90 000 robust measurements for 'fast azimuth', ϕ, and delay time, δt, and 210 000 robust null measurements. Results generally agree with previous work but our measurements allow us to identify hundreds of 'null stations' below which the mantle appears effectively isotropic with respect to azimuthal anisotropy, which are important for some splitting techniques. We make all measurements publicly available as a data product, along with detailed metadata. This serves two purposes: ensuring full reproducibility of results and providing all necessary information for future systematic use of our measurements, in tomography applications or comparisons with geodynamic flow predictions.

Key words: Seismic anisotropy; Dynamics: convection currents, and mantle plumes; Dynamics of lithosphere and mantle; Mantle processes.

1 INTRODUCTION

Seismic anisotropy refers to the phenomenon by which seismic waves travel at different velocities depending on their propagation direction and/or polarization. In the mantle, anisotropy arises due to two primary mechanisms which can both be linked to Earth's internal deformation and convective evolution: (1) Crystallographic-preferred orientation (CPO), where intrinsically anisotropic mineral crystals align under finite deformation with their directional elastic properties, and (2) shape-preferred orientation, involving aligned isotropic or anisotropic materials, for example, layered composites, that can be effectively anisotropic on the scales seen by the dominant seismic wavelength (e.g., Nicolas & Christensen 1987; Silver 1996; Kocks *et al.* 2000; Long & Becker 2010; Romanowicz & Wenk 2017). The detection and characterization of seismic anisotropy can provide valuable information on convective flow in Earth's mantle (e.g., Tanimoto & Anderson 1984; Becker *et al.* 2003; Gaboret *et al.* 2003; Nowacki *et al.* 2011; Wolf *et al.* 2024a). For the typical, 'A' type CPOs of olivine, as they might form under dislocation creep in the upper mantle, the fast propagation direction of upper mantle anisotropy is expected to align with shear in mantle flow. Different alignments might be caused by high volatile and/or stress type CPO formation (e.g., Kneller *et al.* 2005; Lassak *et al.* 2006; Becker *et al.* 2008), although those fabrics appear less common and less systematic in the rock record (e.g., Bernard *et al.* 2019). However, in the deepest mantle, the relationship between anisotropy and flow is more complicated (e.g., Yamazaki & Karato 2001; Wookey & Kendall 2008; Creasy *et al.* 2020); it cannot necessarily be assumed the polarization direction of the fast traveling wave corresponds to the direction of convective flow (e.g., Yamazaki & Karato 2001; Nowacki *et al.* 2011; Wolf & Long 2022). Seismic anisotropy is usually stronger in the upper than in the lowermost mantle (e.g., Romanowicz & Wenk 2017; Becker & Lebedev 2021). Therefore, fast directions of shear wave splitting measurements are routinely interpreted as being due to upper mantle flow (e.g., Silver 1996; Fouch *et al.* 2000; Behn *et al.* 2004; Becker *et al.* 2006).

The SKS, SKKS and PKS (Fig. 1a) seismic phases, hereafter referred to as ∗KS, are SV polarized upon reentry into the mantle from the outer core. If a ∗KS wave travels through an anisotropic region in the receiver-side mantle, it splits into two pulses, one of which travels faster than the other. This phenomenon can occur in Earth's upper mantle, as schematically shown in Fig. 1(b). The two components (red and blue in Fig. 1b) accumulate a time lag, or relative delay time, δt, which increases as a function of the distance traveled through the anisotropic material. We denote the polarization orientation of the fast pulse, or 'fast axis', as ϕ (counted clockwise from the North; Fig. 1c). These two parameters characterize seismic anisotropy for a typical shear wave splitting measurement (Ando *et al.* 1983; Vinnik *et al.* 1984; Silver & Chan 1991).

Shear wave splitting parameters $\{\phi, \delta t\}$ are typically determined through manual or semi-automated inspection and analysis of data (e.g., Teanby *et al.* 2004; Wüstefeld *et al.* 2010, 2008; Reiss & Rümpker 2017), although fully automated approaches have also been applied (e.g., Evans *et al.* 2006; Liu *et al.* 2014; Walpole *et al.* 2014; Link *et al.* 2022; Hudson *et al.* 2023). Results from these manual analyses as well as those derived from automatic approaches have been compiled into large splitting parameter collections (e.g., Silver 1996; Wüstefeld *et al.* 2009). These compilations have provided valuable insights into upper mantle flow and have enabled detailed comparisons between shear-wave splitting (from ∗KS body waves) and surface wave wave inversions (e.g., Montagner *et al.* 2000; Wüstefeld *et al.* 2009; Becker *et al.* 2012). However, global compilations include splitting parameters from studies that use different data processing techniques, which can vary depending on the periods used in analyses and the methods employed to calculate splitting parameters (Savage 1999; Long & van der Hilst 2005; Vecsey *et al.* 2008; Kong *et al.* 2015). Additionally, some studies do not provide specific information on the earthquake data used to determine splitting parameters, making it challenging (if not impossible) to reproduce their results, or to analyze features such as backazimuthal dependence of ϕ and δt which can provide insights into the nature of anisotropy at depth (e.g., Silver & Savage 1994; Rümpker & Silver 1998; Chevrot & van der Hilst 2003).

Here, we automatically measure shear-wave splitting for all earthquakes with magnitudes ≥ 5.9 from the year 2000 to present, which were collected from 24 data centers worldwide. We obtain approximately 90 000 well-constrained sets of $\{\phi, \delta t\}$ pairs and 210 000 null measurements. This automatic measurement database is substantially larger than previous ones (e.g., Liu *et al.* 2014; Walpole *et al.* 2014). The measurements are compared to existing databases and previous automatic splitting efforts and found generally consistent with previous results. We identify hundreds of stations worldwide at which a large majority of ∗KS waves is unsplit, which are called null stations. Null measurements, at which waves appear not influenced by azimuthal seismic anisotropy in the mantle, provide important information (e.g., Wüstefeld & Bokelmann 2007; Walpole *et al.* 2014). Effective 'null stations' are essential for the application of some splitting strategies, such as determining *S*-wave source-side anisotropy (e.g., Russo & Silver 1994; Foley & Long 2011; Lynner & Long 2013), PS bounce point anisotropy (e.g., Wolf *et al.* 2024c), and inferring lowermost mantle anisotropy from ScS and S_{diff} waves (e.g., Wolf *et al.* 2022; Wolf & Long 2024).

The code we use to measure shear-wave splitting is publicly available, and we publish our uniformly processed measurements as well as metadata. This enables reproducibility and the extraction of information such as backazimuthal dependence of splitting parameters. We anticipate that this work will enable new inquiries into Earth's dynamic interior processes using uniformly made measurements from a large global data set.

2 DATA SET AND PRE-PROCESSING

We have collected (and continue collecting) all available data from 24 global data centers from 2000 January 1, to present, for all seismic events with moment magnitudes 5.9 and above (hereafter referred to as the ADEPT data set, http://adept.sese.asu.edu/). We collect 2 hr of data for all stations, instrument deconvolve the data to displacement, rotate the horizontal components to radial and transverse motions, and downsample the seismograms to 20 samples per second. We store the data locally in event-based directories. To date, we have collected over 4700 earthquakes (and over 16 million three-component earthquake recordings). All events and stations that are included in the data set are shown in Fig. 2. The corresponding ∼ 500 seismic networks and their citations are provided in the Supporting Information.

3 SHEAR-WAVE SPLITTING MEASUREMENTS

We conduct shear-wave splitting measurements using the SplitRacerAUTO MATLAB code (Reiss & Rümpker 2017; Link *et al.* 2022). SplitRacerAUTO uses the transverse energy minimization technique (Silver & Chan 1991) with the uncertainty quantification by Walsh *et al.* (2013) to determine ϕ and δt. This is repeated for a certain number (we choose 30) of randomly selected time intervals around the expected phase arrival, and measurements are only used if they are robust across all time windows. The details of this procedure are described in the original publication by Reiss & Rümpker (2017). SplitRacerAUTO additionally calculates the splitting intensity SI (Chevrot 2000), which can be expressed as $\mathrm{SI} \approx \delta t \sin(2(\alpha - \phi))$, where α is the backazimuth for ∗KS phases.

The first step of SplitRacerAUTO is to conduct data preprocessing all selected data. We use PKS waves measured at epicentral distances from their inception and $<155^{\circ}$, SKS at distances $> 85^{\circ}$ to their maximum distance, and SKKS at distances $>100^{\circ}$ to their maximum distance. In the pre-processing, SplitRacerAUTO discards data with low signal-to-noise ratios (SNRs). SNRs are calculated using an effective horizontal component ($\sqrt{R(t)^2 + T(t)^2}$, $R(t)$ = radial component, $T(t)$ = transverse component), and comparing the mean amplitude of a noise window with the signal window. The noise window is 20 s long and ends 5 s prior to the PREM-predicted arrival time. We set an SNR threshold of 2.2 after applying a butterworth bandpass filter of order 2 to retain periods between 6 and 25 s. Next, SplitRacerAUTO uses an additional quality-control

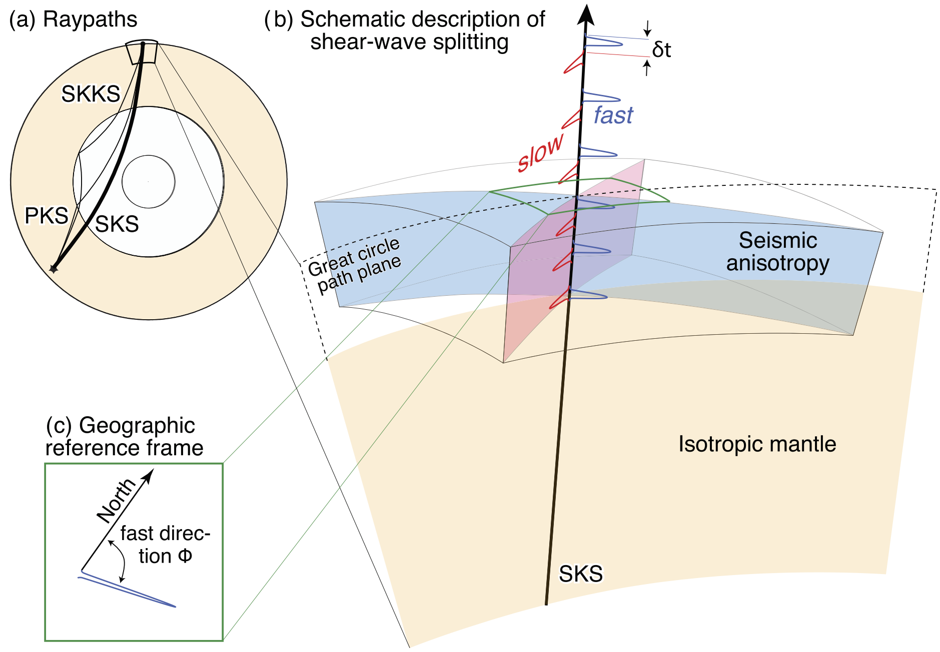

Figure 1. Schematic representation of shear-wave splitting due to upper mantle anisotropy. (a) Schematic Earth cross-section showing PKS, SKS and SKKS (∗KS) ray paths. (b) In presence of seismic anisotropy in the upper mantle, ∗KS splits into fast (blue) and slow (red) traveling components with mutually orthogonal polarizations. These components accumulate a relative time lag (δt); additionally, the fast polarization direction can be measured. (c) Fast polarization direction ϕ relative to geographic north.

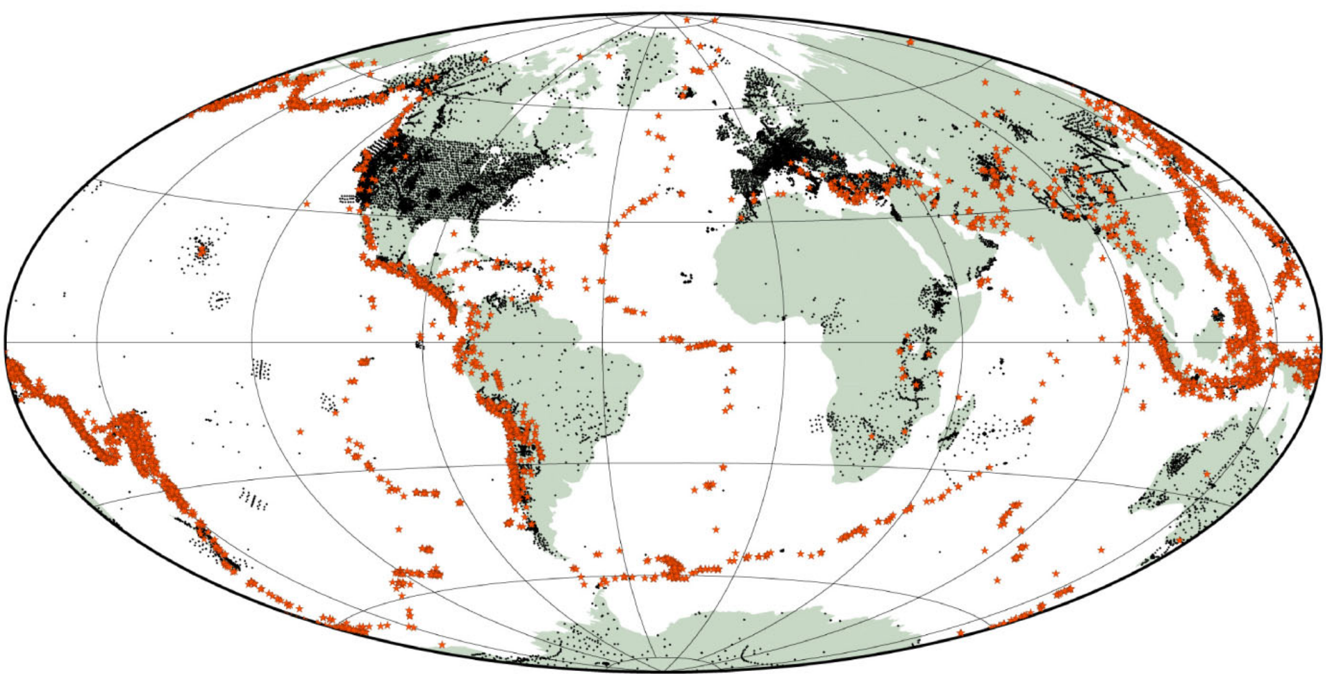

Figure 2. Source–receiver configuration used in this study. Stations are shown as black circles and events as orange stars. We use data from approximately 4700 different events and 25 000 distinct stations.

algorithm to identify the time window in which the ∗KS phase under study arrives, avoiding ∗KS phases that coincide S, ScS and S_{diff} arrivals. In the third step, shear-wave splitting parameters are calculated, and measurements are automatically classified. For more details about SplitRacerAUTO, we refer to Link *et al.* (2022), which includes a thorough benchmark against measurements for which time windows were manually selected and measurements visually classified.

Several modifications have been made to the original code to tailor it for our purposes. We adjust SplitRacerAUTO to read data from event-based directories instead of station-based ones. This data is already rotated into a radial-transverse coordinate frame based on station metadata. To enhance computational speed, which is essential given the large number of seismograms used in this study, we downsample all data to 3 samples per second instead of 20 (that SplitRacerAUTO uses per default). We also found that null measurements can be reliably identified using a single time window. Therefore, if a splitting measurement is null, we do not analyze additional time windows. The same applies if the splitting in the first time window is classified as clearly poor. Although these adjustments are minor and do not impact SplitRacerAUTO's core functionality, they increase computational speeds by a factor of about 200. Our slightly adjusted SplitRacerAUTO version can be found at https://doi.org/10.5281/zenodo.14834413 (Wolf *et al.*, 2025).

Fig. 3 illustrates an example of an SKS shear-wave splitting measurement from data collected at station OJC in Poland, for an event that occurred on 2011 November 22 beneath central Bolivia. In this example, the SKS signal is clearly above the noise level (Fig. 3b), the original particle motion is elliptical, and after correcting for the best-fitting splitting parameters, the particle motion becomes linear (Fig. 3c). The best-fitting $\{\phi,\ \delta t\}$ (Fig. 3d) splitting parameters are tightly constrained.

SplitRacerAUTO assigns several categories to measurements: good, average, null and poor. The criteria used for these categorizations are detailed by Link *et al.* (2022), and we apply the same criteria in this study to assign 'good' and 'average' labels to our $*$KS splitting measurements. These criteria include maximum permissible error bars on δt, minimum required energy reductions for the corrected traces and minimum permissible eigenvalue ratios of the calculated covariance matrix. However, we define null measurements less strictly than Link *et al.* (2022): we label measurements as 'null' if $|\mathrm{SI}| < 0.3$ (instead of < 0.15) and the ratio of the first and second eigenvalues of the covariance matrix is < 0.1 (instead of < 0.06). The decision on how narrowly to define a null measurement is somewhat arbitrary; we adopt this broader SI range for a null definition for practical reasons. Measurements with $|\mathrm{SI}| < 0.3$ do not yield well-constrained $\{\phi,\ \delta t\}$ values because the splitting is too weak (at the periods we are using). Defining these measurements as null allows us to measure splitting for only one time window, thereby not unnecessarily straining our computational resources. In practice, this definition of null measurements has no influence on the determination of null stations, which are often defined by a percentage of unsplit waves measured at them (e.g., Walpole *et al.*, 2014). In this study, we set a higher threshold for the percentage of nulls required to define null stations compared to previous studies. This approach explicitly accounts for weakly split waves that meet our quality criteria but would likely have been discarded as poor in previous studies.

4 RESULTS

4.1 Global splitting measurements

We obtain 64 154 SKS, 14 439 SKKS and 8153 PKS global $\{\phi,\ \delta t\}$ measurements. These results are presented in Fig. 4 in a global overview, and Fig. 5 for regional example zoom-ins.

The overall measurement coverage is largely determined by the station distribution (Fig. 2), and consequently, the availability of publicly accessible seismic data that is part of ADEPT. For example, the measurement density is very high in the United States and Europe, while significantly fewer measurements are available for stations in Russia and India. Outside of Europe and North America, countries such as Chile, Japan, Taiwan, New Zealand, Tajikistan and Kyrgyzstan are particularly well sampled.

4.2 Null measurements

In addition to the splitting parameters $\{\phi,\ \delta t\}$, we identify which measurements are unsplit or null. Stations where a large majority of records show no splitting are often referred to as null stations, yet this is important information, as noted above. We introduce two distinct categories of null stations. If at least 97.5 per cent of the records at a station are unsplit, and the station is sampled from more than one 30°-wide azimuth, the station is assigned a null category label A. If between 95.0 and 97.5 per cent of the measurements are null, the station is classified as category B. For a station to be included in either of these categories, it must have more than 30 null or $\{\phi,\ \delta t\}$ measurements. Fig. 6 shows null stations as colored circles for category A and as gray circles for category B. The color of the circle indicates how many 30° backazimuthal bins (starting at backazimuth = 0°) contain measurements. In total, we identify 178 category A and 371 category B null stations, many of which are located in the United States and Europe (Figs 6b and c).

4.3 Data product description

We make the global $\{\phi,\ \delta t\}$ and null measurements publicly available. For each phase (SKS, SKKS, PKS), we provide a .txt file that includes the following information: event name, for example '200001081647', corresponding to an event that occurred on 2000 January 8 at 4:47pm UTC; event latitude (°); event longitude (°); event depth (km); station name; network name; station latitude (°); station longitude (°); quality tag; δt (s); δt upper error bound (s); δt lower error bound (s); ϕ (°); ϕ upper error bound (°); ϕ lower error bound (°); splitting intensity; splitting intensity upper error bound; splitting intensity lower error bound. These measurements are also available on the data product website associated with this large data collection effort, http://swat.sese.asu.edu. Measurements will occasionally be updated on the website as the ADEPT data set continues to grow.

For each $\{\phi,\ \delta t\}$ and null measurement used in this study, we provide diagnostic splitting plots at http://swat.sese.asu.edu. These graphics, minimally edited from SplitRacerAUTO, include the waveforms, particle motions, $\phi - \delta t$ energy maps (similar to Figs 3b–d) and histograms that show the robustness of the splitting measurements across multiple time windows. These graphical products enable researchers to visually evaluate each splitting measurement for their own use.

Additionally, we include .txt files in the Supporting Information with both category A and B null measurements. The format of these files is: station name, event name, number of robust measurements at the station, station latitude (°), station longitude (°).

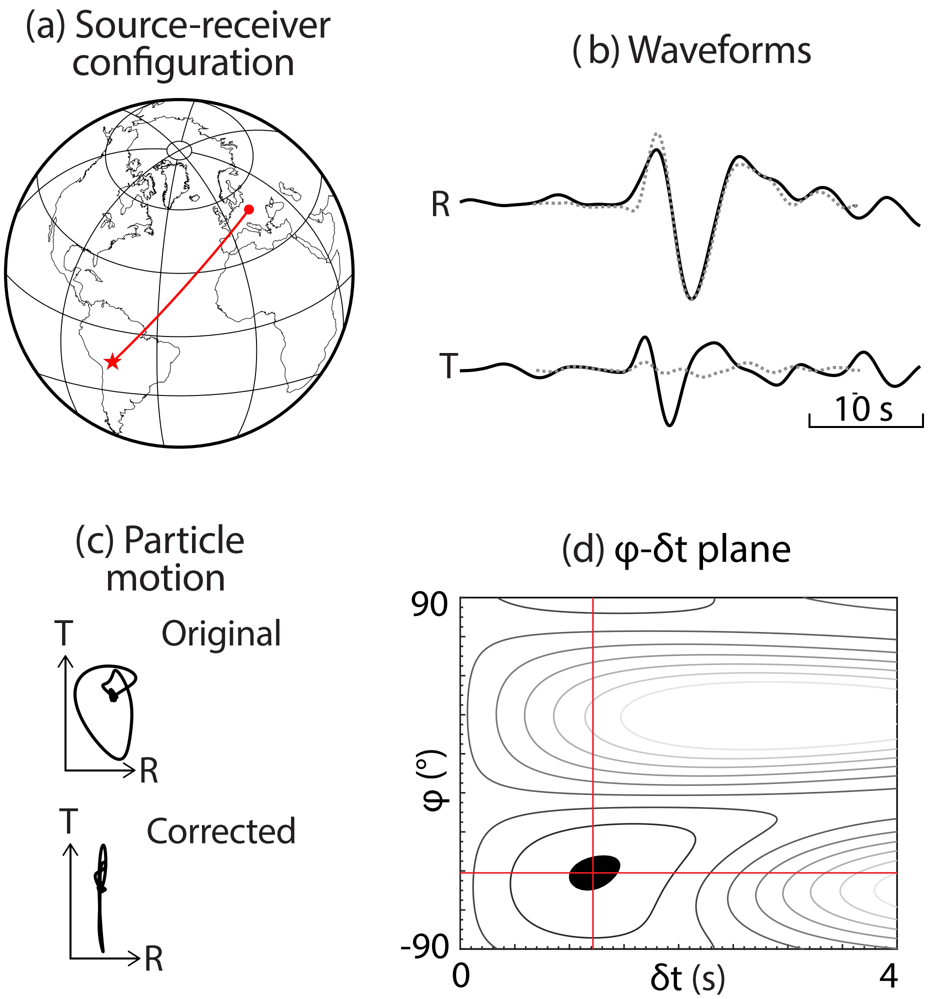

Figure 3. Example of a shear-wave splitting measurement. (a) Event (red star) that occurred on 2011 November 22, beneath central Bolivia and station OJC (red circle) located in Poland. The great-circle path is shown as a red line. (b) Radial (R) and transverse (T) component displacement waveforms. Waveforms corrected for the best-fitting splitting parameters are shown as gray dotted lines. (c) Particle motions (radial versus transverse amplitude) for the original waveform (top) after correction for the best-fitting splitting parameters (bottom). (d) Best-fitting splitting parameters in the ϕ-δt-plane. Black region indicates 95 per cent confidence interval. The best-fitting ϕ and δt values are indicated by a red line. Contour lines show different transverse energy component levels.

5 COMPARISONS TO PREVIOUS STUDIES

5.1 Fast directions and delay times across the continental United States

We focus on the continental United States and its surrounding regions to compare our results with those of previous studies. This region is chosen for its exceptionally dense station coverage, primarily due to the prior deployment of USArray (IRIS Transportable Array 2003), and because several automatic splitting approaches have been applied here (e.g., Liu *et al.* 2014; Walpole *et al.* 2014; Yang *et al.* 2017; Link *et al.* 2022). Specifically, we conduct a detailed comparison of our results with the updated composite compilation of manually picked splitting measurements by Becker *et al.* (2012) which includes the Montpellier database of Wüstefeld *et al.* (2009) with last updates from 2020, and the automatic measurements by Walpole *et al.* (2014) who provided a global database, as well as automated splits from Liu *et al.* (2014) and Yang *et al.* (2017) which are restricted to North America/USArray.

For comparative analysis, we first calculate the station average and then spatially average these splits, but we note that backazimuthal information is retained in the original databases. All averaging is based on delay-time weighted, orientational (i.e. 180° periodic) vector means, and computing the median values within spatial bins. We show 1° × 1° splitting averages for all four approaches in Fig. 7. Results from all compilations or automated approaches display the same overall patterns, but details differ in certain regions. Our measurements (Fig. 7d) generally most resemble those obtained by Liu–Yang (Fig. 7c), whereas there are more differences to the compilation of manually picked measurements (Fig. 7a), as might be expected, and the automated analysis of Walpole *et al.* (2014) (Fig. 7b). The most significant differences from the manual splitting compilation are in the mid United States, where the compilation includes a relatively low number of measurements, whereas the agreement is better on both coasts. Both fast polarization directions and delay times from the manual splitting compilation show less

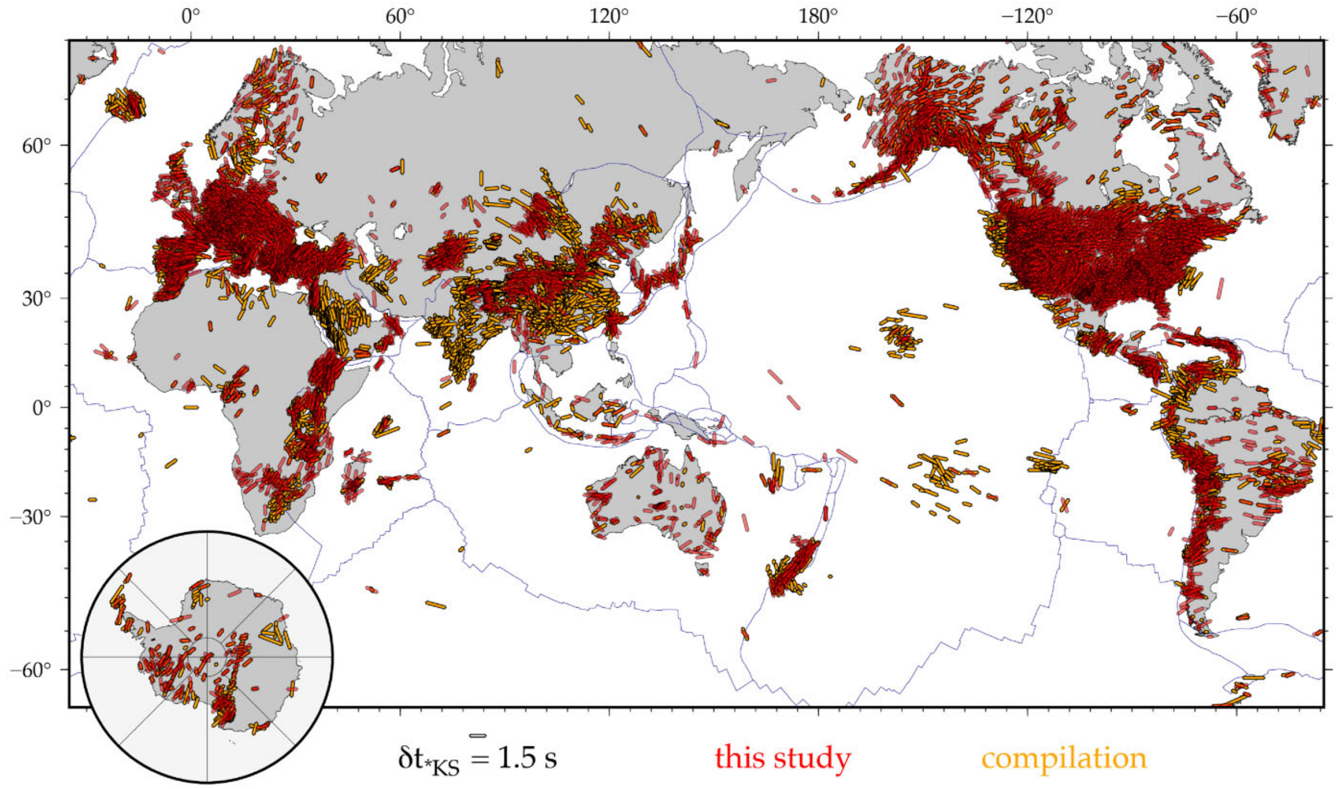

Figure 4. Comparison of global splitting coverage and fast directions between this study (red sticks) and the updated compilation from Becker *et al.* (2012) (orange sticks, including the Montpellier database of Wüstefeld *et al.* (2009) with last updates from 2020), with plate boundaries from Bird (2003) in blue. Results for Antarctica are shown as an inset; see Figs 5 and 7 for regional zoom ins. The compilation includes results from restricted data in China, India and Saudi Arabia, leading to better coverage in these regions. Our study adds more coverage in northern Europe, Australia, southern Africa, central Asia and a stretch of Chile.

smooth patterns compared to the automation-based Wolf and Liu–Yang studies. The fast directions from the Walpole study roughly resemble the other approaches along the west coast of the United States, while agreement is less in the other areas.

We also conduct a statistical comparison between the measurements obtained in this study, the compilation of hand-picked measurements, and the previous Liu–Yang automated splitting measurement approach. The splitting compilation generally shows a broader spread of δt values than Liu and our study using automation-based measurements (Figs 8a, c and d), with Walpole's database showing an even wider spread (Fig. 8b). The mean (expected) value of the delay time distribution are more similar for the compilation and Liu–Yang, with our estimates being $\sim 0.1 - 0.2$ s below those two for North America, and more scatter for Walpole's automated approach. Amplitude differences could potentially be explained by the broader variety of filters used to measure shear-wave splitting for these manually determined measurements. For example, for manual measurements, higher frequencies (up to $\sim$0.5 Hz) can be used to measure δt for low splitting strength and lower frequencies (up to $\sim$0.1 Hz) for larger splitting strengths, whereas we consistently use a bandpass filter between 6 and 25 s (see Section 3). This ensures consistency and comparability among measurements, but may not be ideal for any splitting strength.

We also analyze the differences in ϕ (Figs 8e–h) and δt (Figs 8i–l) across the compilation and the three automated splitting approaches. As suspected based on Fig. 7, the statistical comparison shows that the results from our study are most similar to the Liu's automatic measurement approach. For both ϕ and δt, our results show a slightly greater deviation from the splitting compilation than the previous Liu–Yang automatic approach, while Walpole's estimates show larger deviations, $\sim$twice the mean $\Delta\phi$ deviations from the compilation. Focusing on the difference between our and Liu's approach which are more comparable, those remaining more subtle differences may arise from our choice of a 6 s lower period bound of our bandpass-filter, which is generally higher (in period) than most studies in which splitting measurements are manually determined. Liu *et al.* (2014) and Yang *et al.* (2017) use a lower value of 2 s.

In general, there are multiple potential reasons for the differences between this and the previous studies that used automatic processing compared to the manual splitting compilation. First, data pre-processing varies among studies contributing to the splitting compilation. For instance, different filtering techniques are used on seismic data, and shear-wave splitting can depend on frequency (e.g., Savage 1999; Wüstefeld *et al.* 2008; Wirth & Long 2010). Second, the methods for measuring splitting may differ from the automatic approaches, which both use the transverse energy minimization technique (Silver & Chan 1991). Other methods include the rotation-correlation method (Bowman & Ando 1987) and the multichannel method (Chevrot 2000). These different methods do not always produce identical results (e.g., Savage 1999; Long & van der Hilst 2005; Vecsey *et al.* 2008). Third, some studies determine the incoming backazimuth from the long-axis of the particle motion ellipse at long periods and correct the rotation of the horizontal seismogram accordingly (e.g., Liu & Gao 2013; Wolf & Long 2023). Others (e.g., Ekström & Busby 2008; Reiss *et al.* 2019) determine an average station misorientation and adjust the splitting

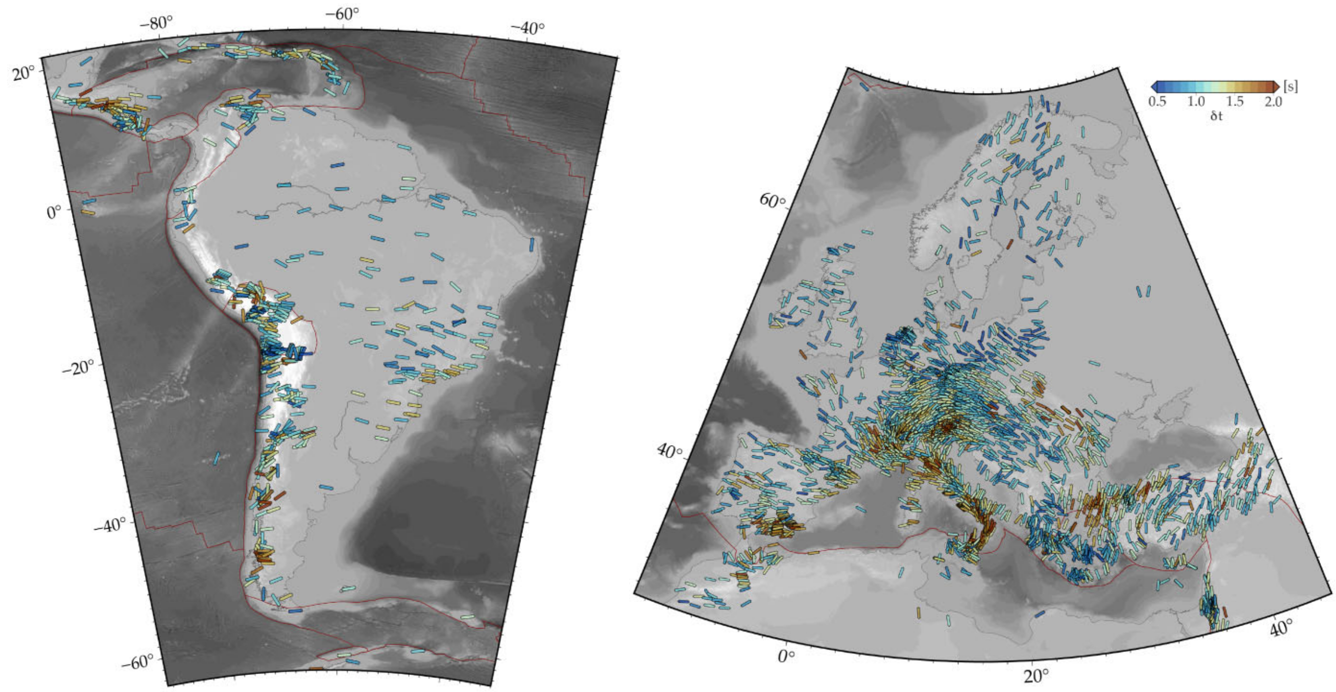

Figure 5. Regional $\{\phi, \delta t\}$ measurement results from our automated analysis for South America (left) and Europe (right). Colored sticks are centered at the station at which splitting was measured. Their orientation indicates the polarization direction ϕ and the color scale represents the delay time δt (legend). Plate boundaries from Bird (2003).

measurements based on that, while again others (e.g., Wolfe & Solomon 1998) rely solely on the station misorientation provided by the data agency. These approaches vary among studies contributing to the splitting compilation. In our study, we determine the incoming backazimuth from the long-period (8–50 s) particle motion and correct the seismogram for a maximum misorientation value of 5°. If the calculated misorientation exceeds this value, no splitting parameters are determined. A systematic comparison of our individual splitting measurements with those from the splitting compilation is not possible, as many previous studies compiled in the compilation do not specify results for individual events at each station.

The Liu–Yang automatic measurements include event information for individual results, which allows us to identify the station-event pairs shared between their studies and ours. Of the 4000 shared station-event pairs, only 15 measurements from Liu–Yang fall outside our 95 per cent confidence intervals for either ϕ or δt. To investigate these 15 pairs in detail, we repeat splitting measurements using the same data processing as described by Liu *et al.* (2014). Specifically, we apply a 2–25 s bandpass-filter and do not correct for the slight backazimuthal difference determined from the long-axis of the particle motion for the individual seismogram. By adopting this approach, we generally replicate results similar to those from Liu–Yang, though minor differences remain that could be caused a slightly different time window selection. An example of this is shown in Fig. S1 of the Supporting Information.

5.2 Global coverage

Fig. 4 compares our uniformly measured data set to the 2024 updated measurement compilation of Becker *et al.* (2012) which includes the database of Wüstefeld *et al.* (2009) updated as of 2020. The Becker compilation contains splitting measurements from restricted data that we do not have access to, for example, in India, China and Saudi Arabia. Therefore, the compilation has much denser coverage in these regions. Compared to the compilation, our measurements add coverage in the central United States, northern Europe, Tajikistan, Kyrgyzstan, Australia and South America. However, this does not necessarily imply that we are the first to measure shear-wave splitting in these regions. Moreover, some existing regional studies are not part of the Wüstefeld *et al.* (2009) or Becker *et al.* (2012) compilations.

Fig. 9(a) compares a generalized spherical harmonics expansion (cf. Becker *et al.* 2007) of a combination of the compilation of Becker *et al.* (2012) and our new automated SKS measurements with surface wave based estimates of azimuthal and radial anisotropy at asthenospheric mantle depths (175 km). As has been discussed widely, patterns of seismic anisotropy in the upper mantle are broadly consistent with convective flow in boundary layers (e.g., Tanimoto & Anderson 1984; Montagner 1998; Becker *et al.* 2008) and SKS splitting fast axes match surface wave based azimuthal anisotropy patterns on the largest scales (Montagner *et al.* 2000; Wüstefeld *et al.* 2009; Becker *et al.* 2012) with remaining debate about the origin of regional deviations even on scales visible on Fig. 9(a).

Fig. 9(b) shows a quantitative comparison in terms of global correlation up to spherical harmonic degree $\ell = 20$, r_{20}. In this update of a similar computation shown in Becker & Lebedev (2021), the match between smoothed SKS and surface wave estimates from SL2013SVA (Schaeffer & Lebedev 2013) and YB13SV (Yuan & Beghein 2013) is improved slightly in the

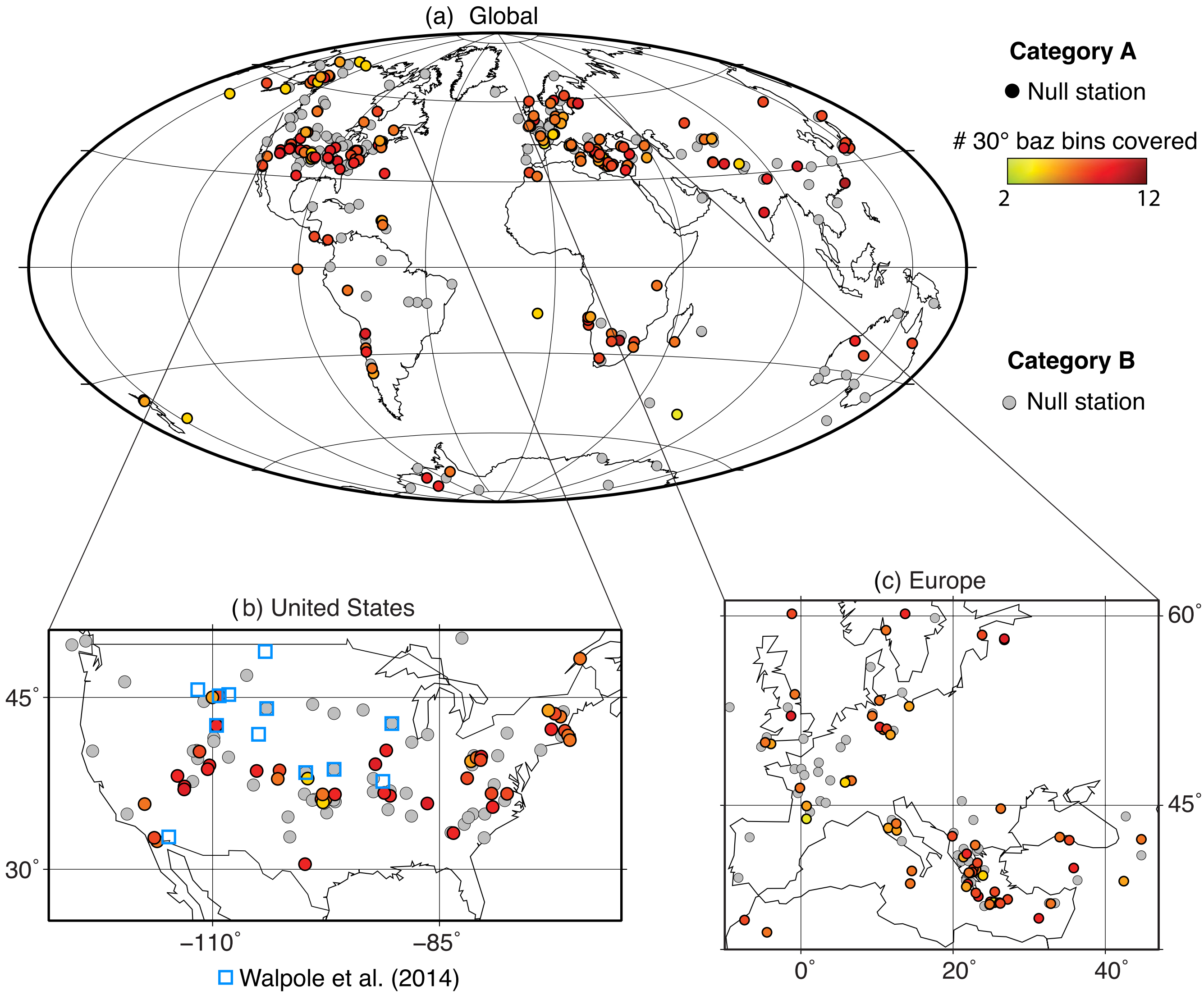

Figure 6. Null stations identified in this study. Category A null stations (stations where > 97.5 per cent of measurements are null, which show sampling from 2 or more 30° backazimuthal bins) are represented as colored circles, the color scale legend indicates the number of 30° backazimuthal bins from which measurements were obtained. Category B null stations (stations having between 95 and 97.5 per cent null measurements) are displayed as gray circles. (a) All null stations. (b) Zoom-in centered on the United States with null stations from Walpole *et al.* (2014) shown as blue squares. (c) Zoom-in centered on Europe.

upper ∼ 300 km of the mantle where we expect CPO formation under dislocation creep to dominate. The comparison with 3D2018 (Debayle *et al.* 2016) shows a statistically significant negative correlation at ∼ 350 km. This is consistent with the comparison of Becker & Lebedev (2021) with an earlier version of the 3D2018 class of models; the physical process causing such a mismatch remain are unclear, with vertical coherence of anisotropy patterns being one possible avenue for further refinement (Yuan & Beghein 2013).

5.3 Null stations

We compare our identified null stations to the previous work of Lynner & Long (2013) and Walpole *et al.* (2014). The reason to use these two studies for comparison is that they used a uniform methodology to identify stations that do not show evidence for ∗KS splitting. In general, our results align more closely with the study of Walpole *et al.* (2014): we also identify 70 per cent of the stations they suggest as null, while this value is below 50 per cent in the Lynner & Long (2013) study. This is likely because the data set used by Walpole *et al.* (2014) is significantly larger than that of Lynner & Long (2013), and therefore more comparable to the data set we are using.

Once again, we focus our detailed comparison on the continental United States and southern Canada (Fig. 6b). In this region, Walpole *et al.* (2014) identified numerous null stations, whereas this area was not the focus of Lynner & Long (2013). The null stations identified by Walpole *et al.* (2014), if not identical, are in the same general regions as those suggested in our study. Walpole *et al.* (2014) does not suggest null stations in the eastern United States because fewer data were available in this region at the time their study was published (Fig. 7b), due to the timing of the USArray deployment.

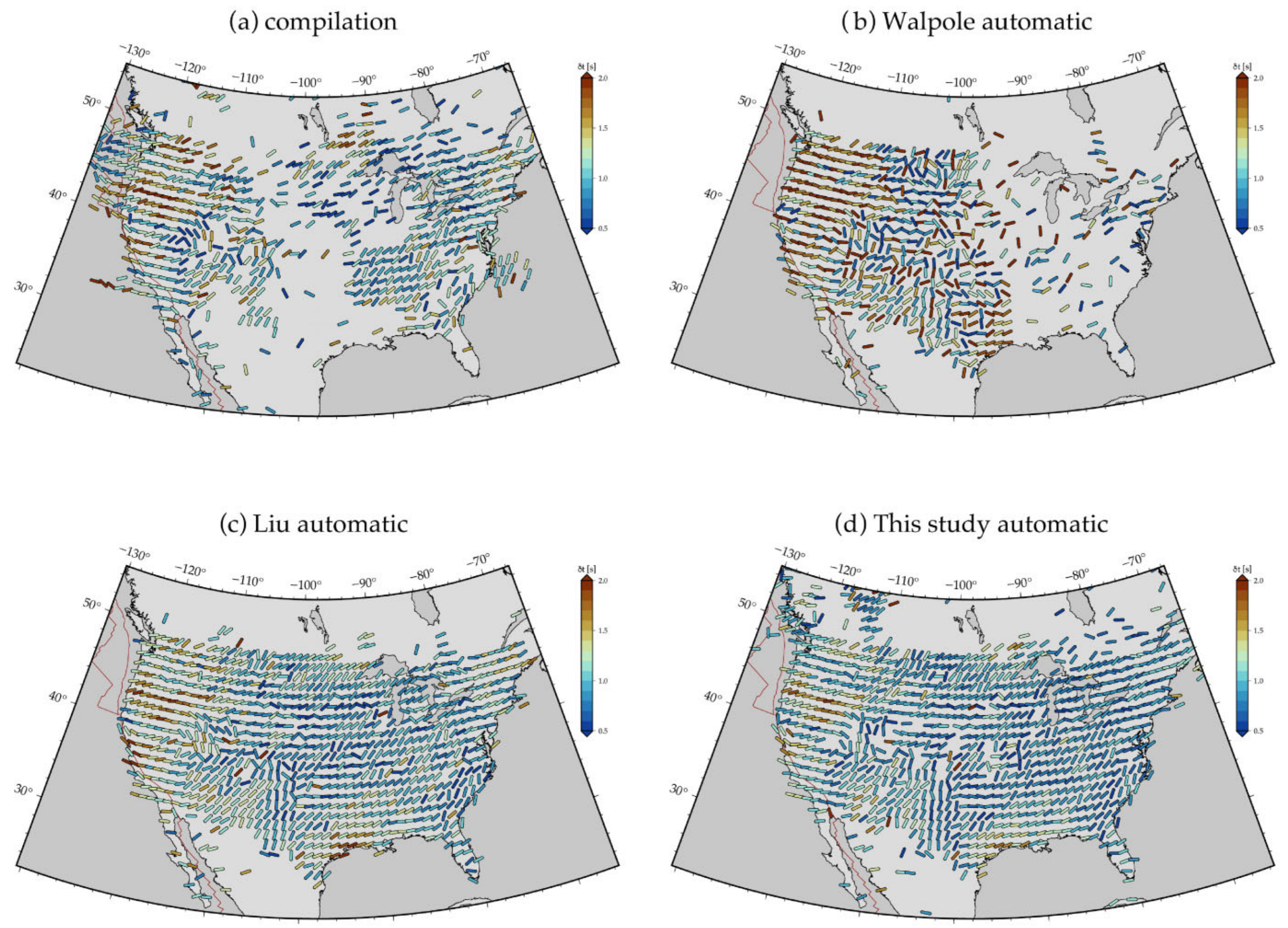

Figure 7. Averaged (1° × 1° bins) shear-wave splitting parameters across the continental United States and the surrounding regions. Results are shown for (a) the updated compilation of manually measured splitting parameters from Becker *et al.* (2012) which includes the Montpellier database of Wüstefeld *et al.* (2009) with last updates from 2020, (b) results from the global automated analysis by Walpole *et al.* (2014), (c) the automatic USArray results from Liu *et al.* (2014) and Yang *et al.* (2017), and, (d) this study. Colored sticks are centered at the station at which splitting was measured. Their orientation indicates the polarization direction ϕ and the color scale represents the delay time δt (legend).

6 DISCUSSION AND CONCLUSION

We have obtained 90 000 $\{\phi, \delta t\}$ and 210 000 null splitting measurements from a seismic data set that currently contains 16 million three-component seismograms. These are six times more measurements than the largest previous uniformly measured compilation of shear-wave splitting measurements (Walpole *et al.* 2014). We have conducted a detailed comparison of our results with previous measurements across the United States. Our automatically determined measurements are very similar to those from Liu *et al.* (2014) and Yang *et al.* (2017), despite the use of different codes. Our results are also generally similar to the compilation of manual splitting results from Becker *et al.* (2012). However, some differences to the splitting compilation exist, which can likely be explained by the fact that the results contained in the compilation were obtained using different processing approaches, and at different seismic periods. We determine hundreds of null stations across the globe which are, in general, agreement with the previous results from Walpole *et al.* (2014).

There are several reasons why we believe that the data product and metadata that we are making publicly available will be a great resource for future research.

(i) The availability of both the metadata and the code package used to conduct the splitting measurements, SplitRacerAUTO (https://www.geophysik.uni-frankfurt.de/64002762/Software), ensures that all results can be reproduced. The code version used in this study is also available at https://doi.org/10.5281/zenodo.14834413 (Wolf *et al.*, 2025).

(ii) Our data set includes measurements from a vast majority of openly accessible high-magnitude seismic event data. Therefore, it will give a good indication of anisotropy patterns in virtually all regions in which open-access data are available, although regional studies may be able to obtain more ∗KS measurements than we present in their particular study region; for example, by including lower-magnitude earthquakes.

(iii) The metadata we provide allow the inference of directional information, which is not always possible in current compilations. Therefore, our measurements can be used to determine changes in

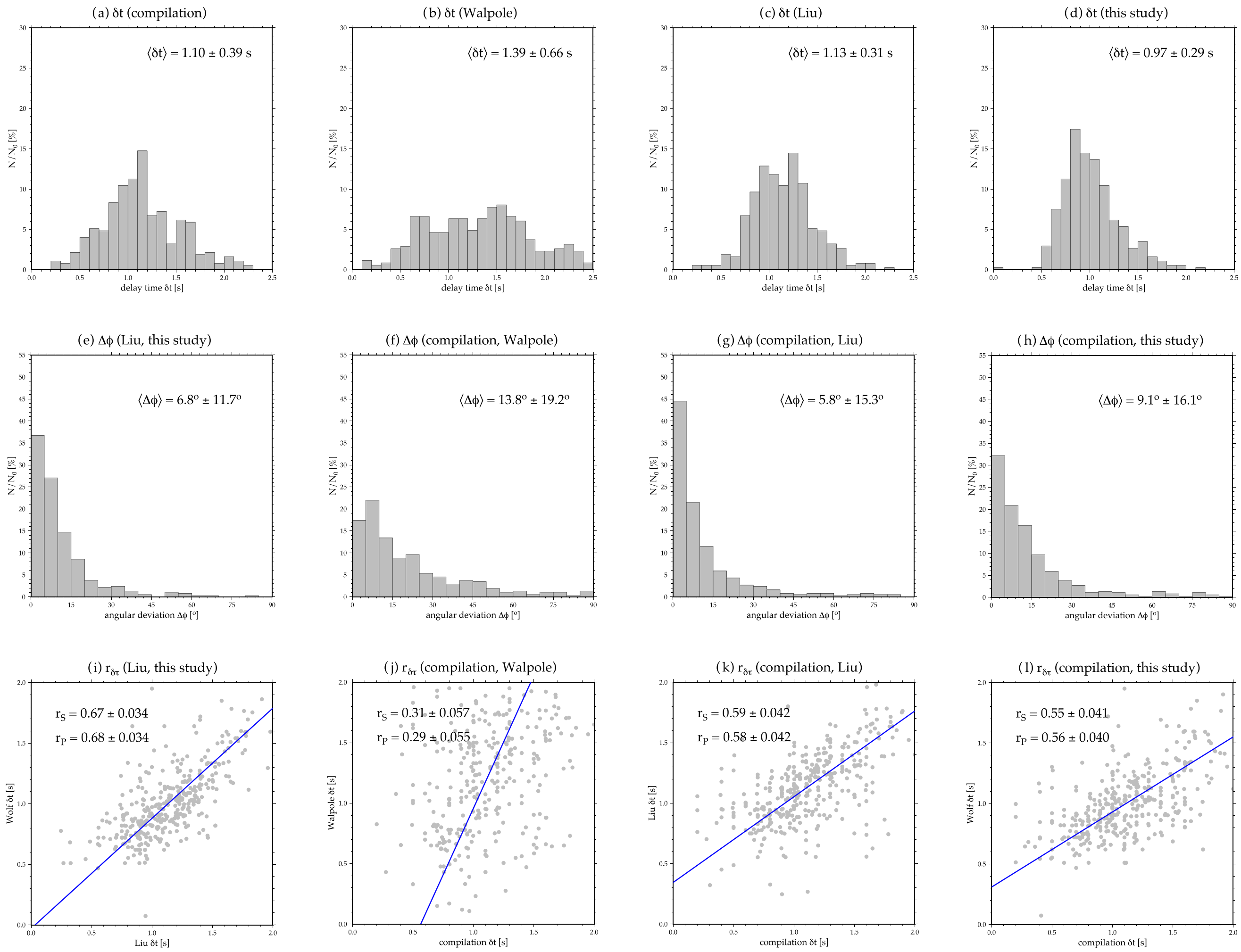

Figure 8. Statistical comparison of the binned splitting results shown in Fig. 7 for North America for regions covered by the respective data sets. 'Compilation' refers to the updated compilation of manual splitting studies from Becker *et al.* (2012), 'Walpole' to the automated measurements of Walpole *et al.* (2014), and 'Liu' to the automatic measurements from Liu *et al.* (2014) and Yang *et al.* (2017). (a–d) Distribution of δt values and mean values ± standard deviation for (a) the compilation of regional studies, and the automated results from (b) Walpole, (c) Liu, and (d) this study. (e–h) Fast polarization differences, $\Delta\phi$ and mean values between pairs of studies: (e) Liu-this study, (f) compilation-Walpole, (g) compilation-Liu, (h) compilation-this study. (i–l) Relationships between delay times δt between the same pairs of studies. The Pearson and Spearman rank correlations are provided as r_{p} and r_{s} with errors from bootstrapping. In general, our results are more similar to the previous automatic measurements of Liu than the compilation, but differences are larger compared to Walpole's automated estimates (not shown) which are also less similar to the compilation.

splitting parameters as a function of backazimuth, which allows detailed regional investigations (e.g., Ritter *et al.* 2022; Fröhlich *et al.* 2024).

(iv) Our measurements have been processed uniformly. For example, we used the same seismic periods for each measurement. This makes it possible to calculate sensitivity kernels as needed for anisotropic tomography approaches (e.g., Chevrot 2006; Link & Long 2024).

(v) We provide an extensive list of null stations, which are crucial to avoid (often unreliable) explicit anisotropy corrections in both investigations of the upper (e.g., Lynner & Long 2013; Wolf & Long 2023) and the lowermost mantle (e.g., Wolf *et al.* 2023, 2024b).

(vi) We make all diagnostic plots publicly available, implying that all measurements and automatic classifications can be individually assessed.

(vii) This data set will be occasionally updated as more seismograms are collected as part of the massive data set collection effort.

ACKNOWLEDGMENTS

JW thanks Barbara Romanowicz and Weiqiang Zhu for their support, and Frederik Link for helpful discussions on SplitRacerAUTO. We thank David Schlaphorst and one anonymous reviewer for constructive feedback. JW was funded by the Miller Institute for Basic Research in Science at UC Berkeley. TWB, EG, KHL and JDW received support from the National Science Foundation via grants nos. EAR-1927216, EAR-1855624, EAR-1853856, EAR-1853911, and EAR-1830644. The Generic Mapping Tools (Wessel & Smith, 1998) and ObsPy (Beyreuther *et al.*, 2010) were used in this research.

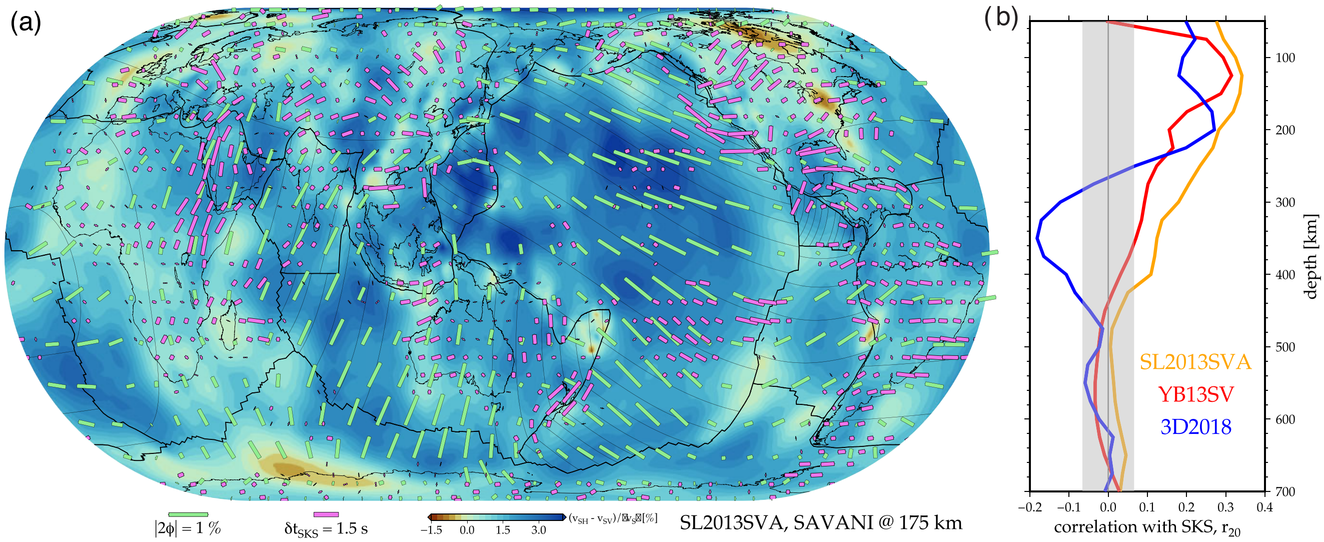

Figure 9. (a) Global upper mantle anisotropy from surface wave inversions and ∗KS splitting. We show radial anisotropy, $\frac{v_{SH}-v_{SV}}{v_S}$, from SAVANI (Auer *et al.* 2014) in the background, and azimuthal anisotropy from SL2013SVA (Schaeffer & Lebedev 2013) (green sticks) at 175 km depth, compared to a spherical harmonics fit of the station averaged SKS results (magenta sticks), up to degree $\ell = 20$ (cf. Becker *et al.* 2007) based on a combination of the Becker *et al.* (2012) compilation plus our new automated splits. Plate boundaries and absolute velocity contours from NUVEL (DeMets *et al.* 1994) in black lines, in the spreading-aligned reference frame of Becker *et al.* (2015), as an approximation of mantle shear (cf. Becker *et al.* 2014). (b) Global correlation up to $\ell = 20$ between the updated SKS expansion and surface wave azimuthal anisotropy models SL2013SVA, YB13SV (Yuan & Beghein 2013) and 3D2018 (Debayle *et al.* 2016). Gray region shows the range outside of which correlations can be considered significant at the 95 per cent confidence level; figure is an update of the comparison shown in Becker & Lebedev (2021).

SUPPORTING INFORMATION

Supplementary data are available at *GJIRAS* online.

Figure S1. Example in which we repeat the approach from Liu *et al.* (2014) to understand cases in which our measurements differ. The example is for station L32A and an event that occurred on 2010 July 23. (a) Measurement using the approach from using a 2–25 s bandpass filter, and not correcting for the difference in back-azimuth for this particular event. Top left: radial (R) and transverse (T) component displacement waveforms. Top right: particle motions (radial versus transverse amplitude) for the original waveform (top) after after correction for the best-fitting splitting parameters (bottom). Bottom: best-fitting splitting parameters in the $\phi - \delta t$-plane. Black region indicates 95 per cent confidence interval. The best-fitting ϕ and δt values are indicated by a red line. Contour lines show different transverse energy component levels. (b) Same plotting conventions as in panel (a) for the approach used in this study. In this and the other (few) cases, when the results from Liu *et al.* (2014) and Yang *et al.* (2017) are outside our ϕ or δt 95 per cent confidence intervals, this can be explained by the differences in data processing.

DATA AVAILABILITY

All data used in this study are publicly available and were collected and pre-processed as part of ASU's global data collection system (http://adept.sese.asu.edu/) for their global data products project (http://swat.sese.asu.edu). Data were collected from the following online data centers: AUSPASS (https://auspass.edu.au/data.html), BGR (https://eida.bgr.de/), CNDC (https://www.earthquakescanada.nrcan.gc.ca/stndon/CNDC/index-en.php), Earthscope (http://service.iris.edu/), ETH (https://eida.ethz.ch/), FNET (https://www.fnet.bosai.go.jp/top.php?LANG=en), GEOFON (https://geofon.gfz-potsdam.de/) (GFZ Data Services 1993), GDMS (https://gdmsn.cwb.gov.tw/) (Central Weather Bureau 2012), ICGC (https://www.icgc.cat/en/Ciutada/Explora-Catalunya/Terratremols), INGV (http://cnt.rm.ingv.it/en/webservices_and_software), IPGP (http://ws.ipgp.fr/) (Institut de physique du globe de Paris (IPGP) & École et Observatoire des Sciences de la Terre de Strasbourg (EOST), 1982), KNMI (http://rdsa.knmi.nl/), KOERI (http://www.koeri.boun.edu.tr/new/en), LMU (http://erde.geophysik.uni-muenchen.de/), NCEDC (https://ncedc.org/) (UC Berkeley Seismological Laboratory 2014), NIEP (https://www.infp.ro/), NOA (http://bbnet.gein.noa.gr/HL/), ORFEUS (http://www.orfeus-eu.org/), RESIF (https://seismology.resif.fr/) (RESIF 1995), SCEDC (https://scedc.caltech.edu/) (Caltech 2014), SSN (http://www.ssn.unam.mx/) (Instituto de Geofísica, Universidad Nacional Autónoma de México, México 2024), TEXNET (http://rtserve.beg.utexas.edu/) and USP (https://sismo.iag.usp.br/). All networks and network citations are included as Supporting Information, and were derived from the FDSN network code list (https://fdsn.org/networks/).

All splitting measurements are available as text files in the Supporting Information. Additionally, measurements can be downloaded at http://swat.sese.asu.edu. Occasional updates will be made available on that website. MATLAB structures with all measurements and matadata that include, for example, the selected time windows and precise event origin times are available at https://doi.org/10.5281/

zenodo.14834413 (Wolf *et al.*, 2025). Splitting measurements from Liu *et al.* (2014), Yang *et al.* (2017) and Walpole *et al.* (2014) are available in the corresponding Supporting Information. The latest splitting compilation update from Becker *et al.* (2012) can be downloaded at https://www-udc.ig.utexas.edu/external/becker/sksdata.html.

CODE AVAILABILITY

SplitRacerAUTO (Link *et al.* 2022) is available at https://www.geophysik.uni-frankfurt.de/64002762/Software. The code version that we used to measure splitting is also available at https://doi.org/10.5281/zenodo.14834413 (Wolf *et al.*, 2025).

REFERENCES

Ando, M., Ishikawa, Y. & Yamazaki, F., 1983. Shear wave polarization anisotropy in the upper mantle beneath Honshu, Japan, *J. Geophys. Res. Solid Earth,* **88**(B7), 5850–5864.

Auer, L., Boschi, L., Becker, T.W., Nissen-Meyer, T. & Giardini, D., 2014. Savani: A variable-resolution whole-mantle model of anisotropic shear-velocity variations based on multiple datasets, *J. Geophys. Res. Solid Earth,* **119,** 3006–3034.

Becker, T.W. & Lebedev, S., 2021. *Dynamics of the Upper Mantle in Light of Seismic Anisotropy, Chap. 10,* pp. 257–282, American Geophysical Union (AGU).

Becker, T.W., Kellogg, J.B., Ekström, G. & O'Connell, R.J., 2003. Comparison of azimuthal seismic anisotropy from surface waves and finite-strain from global mantle-circulation models, *Geophys. J. Int.,* **155,** 696–714.

Becker, T.W., Schulte-Pelkum, V., Blackman, D.K., Kellogg, J.B. & O'Connell, R.J., 2006. Mantle flow under the western United States from shear wave splitting, *Earth planet. Sci. Lett.,* **247,** 235–251.

Becker, T.W., Ekström, G., Boschi, L. & Woodhouse, J., 2007. Length scales, patterns, and origin of azimuthal seismic anisotropy in the upper mantle as mapped by Rayleigh waves, *Geophys. J. Int.,* **171,** 451–462.

Becker, T.W., Kustowski, B. & Ekström, G., 2008. Radial seismic anisotropy as a constraint for upper mantle rheology, *Earth planet. Sci. Lett.,* **267,** 213–237.

Becker, T.W., Lebedev, S. & Long, M.D., 2012. On the relationship between azimuthal anisotropy from shear wave splitting and surface wave tomography, *J. Geophys. Res. Solid Earth,* **117**(B1), B01306, https://doi.org/10.1029/2011JB008705.

Becker, T.W., Conrad, C.P., Schaeffer, A.J. & Lebedev, S., 2014. Origin of azimuthal seismic anisotropy in oceanic plates and mantle, *Earth planet. Sci. Lett.,* **401,** 236–250.

Becker, T.W., Schaeffer, A.J., Lebedev, S. & Conrad, C.P., 2015. Toward a generalized plate motion reference frame, *Geophys. Res. Lett.,* **42**(9), 3188–3196.

Behn, M.D., Conrad, C.P. & Silver, P.G., 2004. Detection of upper mantle flow associated with the African Superplume, *Earth planet. Sci. Lett.,* **224,** 259–274.

Bernard, R., Behr, W.M., Becker, T.W. & Young, D., 2019. Relationships between olivine CPO and deformation parameters in naturally deformed rocks and implications for mantle seismic anisotropy, *Geochem. Geophys. Geosyst.,* **20,** 3469–3494.

Beyreuther, M., Barsch, R., Krischer, L., Megies, T., Behr, Y. & Wassermann, J., 2010. Obspy: A python toolbox for seismology, *Seismol. Res. Lett.,* **81,** 530–533.

Bird, P., 2003. An updated digital model of plate boundaries, *Geochem. Geophys. Geosyst.,* **4**(3), 1–52.

Bowman, J.R. & Ando, M., 1987. Shear-wave splitting in the upper-mantle wedge above the Tonga subduction zone, *Geophys. J. R. Astron. Soc.,* **88,** 25–41.

Caltech, 2014. Southern california earthquake center.

Central Weather Bureau, 2012. Central weather bureau seismographic network, International Federation of Digital Seismograph Networks.

Chevrot, S., 2000. Multichannel analysis of shear wave splitting, *J. Geophys. Res. Solid Earth,* **105,** 21 579–21 590.

Chevrot, S., 2006. Finite-frequency vectorial tomography: a new method for high-resolution imaging of upper mantle anisotropy, *Geophys. J. Int.,* **165,** 641–657.

Chevrot, S. & van der Hilst, R.D., 2003. On the effects of a dipping axis of symmetry on shear wave splitting measurements, *Geophys. J. Int.,* **152,** 497–505.

Creasy, N., Miyagi, L. & Long, M.D., 2020. A library of elastic tensors for lowermost mantle seismic anisotropy studies and comparison with seismic observations, *Geochem. Geophys. Geosyst.,* **21,** e2019GC008883, https://doi.org/10.1029/2019GC008883.

Debayle, E., Dubuffet, F. & Durand, S., 2016. An automatically updated *S*-wave model of the upper mantle and the depth extent of azimuthal anisotropy, *Geophys. Res. Lett.,* **43,** 674–682.

DeMets, C., Gordon, R.G., Argus, D.F. & Stein, S., 1994. Effect of recent revisions to the geomagnetic reversal time scale on estimates of current plate motions, *Geophys. Res. Lett.,* **21,** 2191–2194.

Ekström, G. & Busby, R., 2008. Measurements of seismometer orientation at USarray transportable array and backbone stations, *Seismol. Res. Lett.,* **79,** 554–561.

Evans, M.S., Kendall, J.-M. & Willemann, R.J., 2006. Automated SKS splitting and upper-mantle anisotropy beneath Canadian seismic stations, *Geophys. J. Int.,* **165,** 931–942.

Foley, B.J. & Long, M.D., 2011. Upper and mid–mantle anisotropy beneath the Tonga slab, *Geophys. Res. Lett.,* **38,** 1–5.

Fouch, M.J., Fischer, K.M., Parmentier, E.M., Wysession, M.E. & Clarke, T.J., 2000. Shear wave splitting, continental keels, and patterns of mantle flow, *J. Geophys. Res. Solid Earth,* **105,** 6255–6275.

Fröhlich, Y., Grund, M. & Ritter, J.R.R., 2024. Lateral and vertical variations of seismic anisotropy in the lithosphere–asthenosphere system underneath Central Europe from long-term splitting measurements, *Geophys. J. Int.,* **239,** 112–135.

Gaboret, C., Forte, A.M. & Montagner, J.-P., 2003. The unique dynamics of the Pacific hemisphere mantle and its signature on seismic anisotropy, *Earth planet. Sci. Lett.,* **208,** 219–233.

GFZ Data Services, 1993. GEOFON data centre: GEOFON seismic network.

Hudson, T., Asplet, J. & Walker, A., 2023. Automated shear-wave splitting analysis for single- and multi-layer anisotropic media, *Seismica,* **2,** 1–19.

Institut de physique du globe de Paris (IPGP)& École et Observatoire des Sciences de la Terre de Strasbourg (EOST), 1982. Geoscope, french global network of broad band seismic stations.

Instituto de Geofisica, Universidad Nacional Autónoma de México, México, 2024. SSN: Servicio Sismológico Nacional.

IRIS Transportable Array, 2003. USArray Transportable Array.

Kneller, E.A., van Keken, P.E., Karato, S. & Park, J., 2005. B-type olivine fabric in the mantle wedge: insights from high-resolution non-Newtonian subduction zone models, *Earth planet. Sci. Lett.,* **237,** 781–797.

Kocks, U., Tomé, C. & Wenk, H., 2000. *Texture and Anisotropy: Preferred Orientations in Polycrystals and Their Effect on Materials Properties,* Cambridge University Press.

Kong, F., Gao, S.S. & Liu, K.H., 2015. A systematic comparison of the transverse energy minimization and splitting intensity techniques for measuring shear-wave splitting parameters, *Bull. seism. Soc. Am.,* **105,** 230–239.

Lassak, T.M., Fouch, M.J., Hall, C.E. & Kaminski, É., 2006. Seismic characterization of mantle flow in subduction systems: can we resolve a hydrated mantle wedge?, *Earth planet. Sci. Lett.,* **243,** 632–649.

Link, F. & Long, M.D., 2024. SItomo—a toolbox for splitting intensity tomography and application in the Eastern Alps, *J. Geodyn.,* **159,** 102 018, https://doi.org/10.1016/j.jog.2024.102018.

Link, F., Reiss, M.C. & Rümpker, G., 2022. An automatized XKS-splitting procedure for large data sets: extension package for SplitRacer and application to the USArray, *Comput. Geosci.,* **158,** 104 961, https://doi.org/10.1016/j.cageo.2021.104961.

Liu, K. *et al.*, 2014. A uniform database of teleseismic shear wave splitting measurements for the western and central United States, *Geochem. Geophys. Geosyst.,* **15,** 2075–2085.
Liu, K.H. & Gao, S.S., 2013. Making reliable shear–wave splitting measurements, *Bull. seism. Soc. Am.,* **103**(5), 2680–2693.
Long, M.D. & Becker, T., 2010. Mantle dynamics and seismic anisotropy, *Earth planet. Sci. Lett.,* **297,** 341–354.
Long, M.D. & van der Hilst, R.D., 2005. Upper mantle anisotropy beneath japan from shear wave splitting, *Phys. Earth planet. Inter.,* **151**(3), 206–222.
Lynner, C. & Long, M.D., 2013. Sub-slab seismic anisotropy and mantle flow beneath the Caribbean and Scotia subduction zones: effects of slab morphology and kinematics, *Earth planet. Sci. Lett.,* **361,** 367–378.
Montagner, J.-P., 1998. Where can seismic anisotropy be detected in the Earth's mantle? In boundary layers, *Pure appl. Geophys.,* **151,** 223–256.
Montagner, J.-P., Griot-Pommera, D.-A. & Lavé, J., 2000. How to relate body wave and surface wave anisotropy?, *J. Geophys. Res. Solid Earth,* **105,** 19 015–19 027.
Nicolas, A. & Christensen, N.I., 1987. Formation of anisotropy in upper mantle peridotites; a review, in *Composition, Structure and Dynamics of the Lithosphere-Asthenosphere System,* Vol. **16,** pp. 111–123, eds Fuchs, K. & Froidevaux, C., American Geophysical Union, Washington DC.
Nowacki, A., Wookey, J. & Kendall, J.-M., 2011. New advances in using seismic anisotropy, mineral physics and geodynamics to understand deformation in the lowermost mantle, *J. Geodyn.,* **52,** 205–228.
Reiss, M. & Rümpker, G., 2017. SplitRacer: MATLAB Code and GUI for semiautomated analysis and interpretation of teleseismic shear–wave splitting, *Seismol. Res. Lett.,* **88,** 392–409.
Reiss, M.C., Long, M.D. & Creasy, N., 2019. Lowermost mantle anisotropy beneath Africa from differential SKS-SKKS shear-wave splitting, *J. Geophys. Res. Solid Earth,* **124**(8), 8540–8564.
RESIF, 1995. RESIF-RLBP French broad-band network, RESIF-RAP strong motion network and other seismic stations in metropolitan France.
Ritter, J., Froehlich, Y., Alonso, Y. & Grund, M., 2022. Short-scale laterally varying SK(K)S shear wave splitting at BFO, Germany–implications for the determination of anisotropic structures, **26,** *J. Seismol.,* 1137–1156.
Romanowicz, B. & Wenk, H.-R., 2017. Anisotropy in the deep Earth, *Phys. Earth planet. Inter.,* **269,** 58–90.
Rümpker, G. & Silver, P.G., 1998. Apparent shear-wave splitting parameters in the presence of vertically varying anisotropy, *Geophys. J. Int.,* **135,** 790–800.
Russo, R.M. & Silver, P.G., 1994. Trench-parallel flow beneath the Nazca plate from seismic anisotropy, *Science,* **263**(5150), 1105–1111.
Savage, M.K., 1999. Seismic anisotropy and mantle deformation: what have we learned from shear wave splitting?, *Rev. Geophys.,* **37,** 65–106.
Schaeffer, A. & Lebedev, S., 2013. Global shear speed structure of the upper mantle and transition zone, *Geophys. J. Int.,* **194,** 417–449.
Silver, P.G., 1996. Seismic anisotropy beneath the continents: probing the depths of geology, *Annu. Rev. Earth Planet. Sci.,* **24**(1), 385–432.
Silver, P.G. & Chan, W.W., 1991. Shear wave splitting and subcontinental mantle deformation, *J. Geophys. Res. Solid Earth,* **96,** 16 429–16 454.
Silver, P.G. & Savage, M.K., 1994. The interpretation of shear-wave splitting parameters in the presence of two anisotropic layers, *Geophys. J. Int.,* **119,** 949–963.
Tanimoto, T. & Anderson, D.L., 1984. Mapping convection in the mantle, *Geophys. Res. Lett.,* **11,** 287–290.
Teanby, N.A., Kendall, J.-M. & Van der Baan, M., 2004. Automation of shear-wave splitting measurements using cluster analysis, *Bull. seism. Soc. Am.,* **94,** 453–463.
UC Berkeley Seismological Laboratory, 2014. Northern California earthquake data center.
Vecsey, L., Plomerová, J. & Babuška, V., 2008. Shear-wave splitting measurements—problems and solutions, *Tectonophysics,* **462**(1), 178–196.
Vinnik, L., Kosarev, G.L. & Makeyeva, L.I., 1984. Anisotropy of the lithosphere from the observations of SKS and SKKS phases, *Proc. Acad. Sci. USSR,* **278,** 1335–1339.
Walpole, J., Wookey, J., Masters, G. & Kendall, J.M., 2014. A uniformly processed data set of SKS shear wave splitting measurements: a global investigation of upper mantle anisotropy beneath seismic stations, *Geochem. Geophys. Geosyst.,* **15,** 1991–2010.
Walsh, E., Arnold, R. & Savage, M.K., 2013. Silver and Chan revisited, *J. Geophys. Res. Solid Earth,* **118,** 5500–5515.
Wessel, P. & Smith, W.H.F., 1998. New improved version of generic mapping tools released, *EOS, Trans. Am. geophys. Un.,* **79,** 579–579.
Wirth, E. & Long, M.D., 2010. Frequency-dependent shear wave splitting beneath the Japan and Izu-Bonin subduction zones, *Phys. Earth planet. Inter.,* **181**(3), 141–154.
Wolf, J. & Long, M., 2024. ScS shear-wave splitting in the lowermost mantle: practical challenges and new global measurements, *Seismica,* **3,** 1–21.
Wolf, J. & Long, M.D., 2022. Slab-driven flow at the base of the mantle beneath the northeastern Pacific Ocean, *Earth planet. Sci. Lett.,* **594,** 117 758, https://doi.org/10.1016/j.epsl.2022.117758.
Wolf, J. & Long, M.D., 2023. Upper mantle anisotropy and flow beneath the pacific ocean revealed by differential PS-SKS splitting, *Geophys. Res. Lett.,* **50**(16), e2023GL104402, https://doi.org/10.1029/2023GL104402.
Wolf, J., Long, M.D., Leng, K. & Nissen-Meyer, T., 2022. Constraining deep mantle anisotropy with shear wave splitting measurements: challenges and new measurement strategies, *Geophys. J. Int.,* **230,** 507–527.
Wolf, J., Long, M.D., Creasy, N. & Garnero, E., 2023. On the measurement of Sdiff splitting caused by lowermost mantle anisotropy, *Geophys. J. Int.,* **233,** 900–921.
Wolf, J., Li, M., Long, M.D. & Garnero, E., 2024a. Advances in mapping lowermost mantle convective flow with seismic anisotropy observations, *Rev. Geophys.,* **62,** e2023RG000833, https://doi.org/10.1029/2023RG000833.
Wolf, J., Long, M.D. & Frost, D.A., 2024b. Ultralow velocity zone and deep mantle flow beneath the Himalayas linked to subducted slab, **17,** *Nat. Geosci.,* 1–7.
Wolf, J., Long, M.D., Frost, D.A. & Nissen-Meyer, T., 2024c. The expression of mantle seismic anisotropy in the global seismic wavefield, *Geophys. J. Int.,* **238,** 346–363.
Wolf, J., Becker, T.W., Garnero, E., Liu, K.H. & West, J.D., 2025. Additional data/codes concerning "Comprehensive global dataset of uniformly processed shear-wave splitting measurements", *Zenodo*.
Wolfe, C.J. & Solomon, S.C., 1998. Shear-wave splitting and implications for mantle flow beneath the MELT region of the East Pacific rise, *Science,* **280**(5367), 1230–1232.
Wookey, J. & Kendall, J.-M., 2008. Constraints on lowermost mantle mineralogy and fabric beneath Siberia from seismic anisotropy, *Earth planet. Sci. Lett.,* **275,** 32–42.
Wüstefeld, A. & Bokelmann, G., 2007. Null detection in shear-wave splitting measurements, *Bull. seism. Soc. Am.,* **97,** 1204–1211.
Wüstefeld, A., Bokelmann, G., Zaroli, C. & Barruol, G., 2008. Splitlab: a shear-wave splitting environment in MATLAB, *Comput. Geosci.,* **34,** 515–528.
Wüstefeld, A., Bokelmann, G.H.R., Barruol, G. & Montagner, J.-P., 2009. Identifying global seismic anisotropy patterns by correlating shear-wave splitting and surface-wave data, *Phys. Earth planet. Inter.,* **176,** 198–212.
Wüstefeld, A., Al-Harrasi, O., Verdon, J.P., Wookey, J. & Kendall, J.M., 2010. A strategy for automated analysis of passive microseismic data to image seismic anisotropy and fracture characteristics, *Geophys. Prospect.,* **58**(5), 755–773.
Yamazaki, D. & Karato, S., 2001. High-pressure rotational deformation apparatus to 15 GPa, *Rev. Sci. Instrum.,* **72,** 4207–4211.
Yang, B., Liu, Y., Dahm, H., Liu, K. & Gao, S., 2017. Seismic azimuthal anisotropy beneath the eastern United States and its geodynamic implications, **44,** *Geophys. Res. Lett.,* 2670–2678.
Yuan, K. & Beghein, C., 2013. Seismic anisotropy changes across upper mantle phase transitions, *Earth planet. Sci. Lett.,* **374,** 132–144.